From quantum dots to quantum dashes: Excitonic spectra of highly elongated InAs/InP nanostructures

M. Zieliński*

Institute of Physics, Faculty of Physics, Astronomy and Informatics, Nicolaus Copernicus University, Grudziadzka 5, 87-100 Torun, Poland

(Received 23 August 2018; revised manuscript received 28 March 2019; published 1 May 2019)

A transition from a cylindrical quantum dot to a highly elongated quantum dash is theoretically studied here with an atomistic approach combining empirical tight binding for single particle states and a configuration interaction method for excitonic properties. Large nanostructure shape anisotropy leads to a peculiar trend of bright exciton splitting, which is quenched at a certain point with further shape elongation, contradicting predictions of simplified models. Moreover, strong shape elongation promotes pronounced optical activity of the dark exciton, which can reach a substantial 1% of the bright exciton intensity without application of any external fields. An atomistic calculation is augmented with an elementary phenomenological model expressed in terms of light-hole exciton admixture increasing with shape deformation. Also, excitonic complexes X^-, X^+, and XX are studied, and the correlations due to the presence of higher excited states are identified as key factors affecting excitonic binding energies and the fine structure.

DOI: 10.1103/PhysRevB.99.205402

I. INTRODUCTION

Self-assembled InAs/InP nanostructures are promising quantum emitters at 1.3 or 1.55 μm telecom wavelengths [1–4]. Potential applications of these systems involve single photons and entangled photons generation [5–8] in quantum information and quantum communication [9–11]. The realm of InAs/InP nanostructures is rich and varies from more conventional cylindrical self-assembled [12,13] and nanowire quantum dots [14–16] to rather unconventional semiconductor nanostructures with characteristic large in-plane elongation, known as quantum dashes [17–27]. Quantum dashes have demonstrated their potential for utilization in lasers, amplifiers [19,20,28], and single photon emitters [29,30]. Quantum dashes have also demonstrated significant tuning capabilities through embedding in photonic mesas [31], and they have demonstrated several unique properties, such as suppression of phonon-induced decoherence [26].

Recently, by application of an external magnetic field, quantum dashes [32] have demonstrated their capability of systematically reducing bright exciton fine structure splitting [33–35] below the natural linewidth of emission, which makes quantum dashes a prospective source of polarization entangled photon pairs from biexciton-exciton cascade [7]. The reduction of the fine structure splitting aimed towards entanglement generation is an important scientific topic, and significant efforts have been made to achieve this goal, including, among many others, post-growth annealing [36,37], spectral filtering [38], sample selection [39,40], growth of high symmetry structures [13,15,41–43], and the application of external electric [44,45], magnetic [8,46,47], and strain fields [48–50]. It is thus of practical importance to study the bright exciton fine structure splitting in quantum dot-quantum dash systems and see how it evolves with deformation for high-aspect ratio structures. At the other end of excitonic spectra, there are the dark exciton states, which recently gained attention for their potential as long-lived yet optically addressable quantum bits [51–53] or as auxiliary (metastable) states for the time-bin entanglement generation scheme [54,55]. For the same reasons, the biexciton spectra is also particularly interesting, so we have studied dark exciton and several excitonic complexes, such as biexciton, and this paper presents the results in detail.

Apart from any practical utilization, quantum dashes are intriguing from a basic scientific point of view. For example, it is curious how single particle and many body properties evolve from having the characteristics of a cylindrical quantum dot to a high-aspect ratio, deformed quantum dash by gradual deformation of nanostructure shape. Such an observation is typically not directly experimentally possible, but it is fully attainable in a theoretical study, which by its nature focuses on individual, single quantum systems of well-defined size, shape, and composition. Further, experiments are often hindered by uncertainties due to inhomogeneous broadening in ensemble studies [56] or unavoidable alloy randomness effects originating from the specifics of epitaxial growth [56,57], particularly growth on mixed composition substrates (e.g., InGaAlAs [27,58]). A detailed knowledge of nanostructure morphology (chemical composition, intermixing, actual dimensions) is often very difficult if not impossible to obtain [17,18,21,59]. Theoretical simulation can filter out these difficulties to a certain degree by focusing not on direct comparison with a particular quantum dash or quantum dot experiment but rather analyzing general trends with shape elongation. Utilization of an accurate approach (e.g., atomistic) should however give hope to producing results consistent with and supporting of experimental findings. Moreover, theoretical studies should also give insight into future applications such as intentional tailoring of high-aspect ratio nanostructures

*mzielin@fizyka.umk.pl

to match spectral features demanded in the broad field of nanophotonics [60–63].

The focus of this paper is on the details of the InAs/InP quantum dot-quantum dash single exciton spectra and particularly fine structure splitting and bright and dark exciton optical activity, all calculated as a function of shape deformation from high rotational shape symmetry to high-aspect ratio elongation. Spectra of several excitonic complexes, i.e., the negatively and positively charged exciton and the biexciton, are studied here as well. For all these cases, this paper underlines the key role of correlation effects due to the presence of higher levels (configuration mixing) affecting all major features of quantum dashes excitonic spectra significantly.

System and methods

In this work, we study InAs nanostructures elongated from an ideal disk-shape quantum dot to a highly-elongated (nanorodlike) elliptical quantum dash. The height of all deformed nanostructures is kept fixed at 3 nm. The diameter in a fully cylindrical case is 20.6 nm (radius $r = 10.3$ nm). These dimensions are typical for self-assembled quantum dots and quantum dashes [21]. In our previous work [56], we studied the effects of nanostructure size and composition on quantum dash spectra; here, we focus on the role of lateral deformation for pure InAs/InP systems. Anisotropy is applied by elongating the system along the [1$\underline{1}$0] axis and shrinking it in the perpendicular [110] axis at the same time, such that the base field (and the overall dot volume) is kept constant. The elongation axis was chosen as [1$\underline{1}$0], which is consistent with experimental findings [64]. The elongation is governed by anisotropy [35,65,66] parameter t with a longer axis (major) with length given by $X = r \times (1 + t)$ and a shorter axis (minor) with length given by $Y = r/(1 + t)$. We consider t to vary from 0 to 2.0 (Fig. 1), so the aspect ratio (X/Y) is given as $(1 + t)^2$ and reaches 9 for the highest deformation considered. The nanostructure is located on a 1 lattice with a constant (2 monolayers) thickness (0.6 nm) InAs wetting layer [67] and embedded in an InP barrier. The symmetry in all cases is C_{2v}, even for the $t = 0$ case, due to the presence of the wetting layer [66] and the lack of a "rotoinversion operation" [41]. Since t was varied from 0 to 2.0 with a step size of 0.1, the calculations were performed for a total of 21 different systems.

The calculation starts with finding atomic positions that minimize total elastic energy. This is done by using the valence force field method of Keating [68,69] with a cylindrical

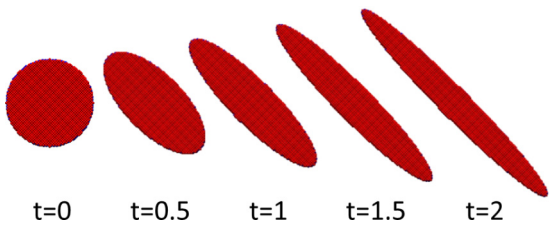

FIG. 1. Schematics (top view) of InAs nanostructure shape deformation along the [1$\underline{1}$0] crystal axis as a function t for several arbitrarily chosen values. The InAs wetting layer below the nanostructure and the surrounding InP barrier are omitted for clarity.

computational box containing over 32 million atoms and minimization of strain energy is performed using the conjugate gradient method [70]. The valence force method is described in more detail in Refs. [71,72] and in our previous papers [70,73–75]. Next, from atomic positions, the piezoelectric potential [76–80] is calculated by accounting for both linear and quadratic contributions [81].

Then, the single particle spectra of electrons and holes are obtained with the empirical tight-binding method accounting for d-orbitals and spin-orbit interaction [74,75]. The single-particle tight-binding Hamiltonian for the system of N atoms and m orbitals per atom can be written in the language of the second quantization as follows [73]:

$$\hat{H}_{TB} = \sum_{i=1}^{N}\sum_{\alpha=1}^{m} E_{i\alpha} c_{i\alpha}^{+} c_{i\alpha} + \sum_{i=1}^{N}\sum_{\alpha=1,\beta=1}^{m} \lambda_{i\alpha,\beta} c_{i\alpha}^{+} c_{i\beta} + \sum_{i=1}^{N}\sum_{j=1}^{\text{near.neigh.}}\sum_{\alpha,\beta=1}^{m} t_{i\alpha,j\beta} c_{i\alpha}^{+} c_{j\beta}, \quad (1)$$

where $c_{i\alpha}^{+}$ ($c_{i\alpha}$) is the creation (annihilation) operator of a carrier on the (spin-)orbital α localized on the site i, $E_{i\alpha}$ is the corresponding on-site (diagonal) energy, and $t_{i\alpha,j\beta}$ describes the hopping (off-site and off-diagonal) of the particle between the orbitals on the four nearest neighboring sites. i iterates over all atoms, whereas j iterates over the four nearest neighbors only. α is a composite (spin and orbital) index of the on-site orbital, whereas β is a composite index of the neighboring atom orbital. Coupling to further neighbors is thus neglected, and $\lambda_{i\alpha,\beta}$ (on-site and off-diagonal) accounts for the spin-orbit interaction following the description given by Chadi [82], which includes the contributions from atomic p orbitals.

Here, we use the $sp^3d^5s^*$ parametrization of Jancu [83]. The tight-binding calculation is effectively performed on a smaller domain than the valence force field calculation [84,85], but the number of atoms in the tight-binding computational box still exceeds 1.3 million, which presents a substantial numerical problem. The details of the $sp^3d^5s^\star$ tight-binding calculation were discussed thoroughly in our earlier papers [70,73–75].

Finally, the excitonic spectra are calculated with the configuration interaction method. The Hamiltonian for the interacting electrons and holes can be written in second quantization as follows [86]:

$$\hat{H}_{ex} = \sum_i E_i^e c_i^\dagger c_i + \sum_i E_i^h h_i^\dagger h_i + \frac{1}{2}\sum_{ijkl} V_{ijkl}^{ee} c_i^\dagger c_j^\dagger c_k c_l + \frac{1}{2}\sum_{ijkl} V_{ijkl}^{hh} h_i^\dagger h_j^\dagger h_k h_l - \sum_{ijkl} V_{ijkl}^{eh,\text{dir}} c_i^\dagger h_j^\dagger h_k c_l + \sum_{ijkl} V_{ijkl}^{eh,\text{exchg}} c_i^\dagger h_j^\dagger c_k h_l, \quad (2)$$

where E_i^e and E_i^h are the single particle electron and hole energies obtained at the single particle stage of calculations, respectively, and V_{ijkl} are Coulomb matrix elements (Coulomb direct and exchange integrals) calculated according to the procedure given in Ref. [73]. More details on Coulomb

matrix element computation for tight-binding wave functions can also be found in Refs. [87,88] as well as in our recent work in Ref. [89].

Typically, only s, p, and d single particle shells are included in the configuration interaction calculation of quantum dot electronic spectra [73,90]. In this work, we go beyond this approximation and account for the f shell as well, resulting in a total of 20 electron (with spin) and 20 hole single particle states entering many-body calculations and a total of over 0.6 million Coulomb direct and exchange integrals calculated over 1.3 million atoms in the computational box [73,89]. Thus, calculation of the multiexcitonic spectra produces a significant computational challenge, and on a 192-core computer cluster, it takes approximately 72 hours for all computational stages combined (i.e., strain, piezoelectricity, tight-binding, and configuration interaction) for every t value, where the configuration interaction is by far the most time-demanding part.

II. SINGLE PARTICLE SPECTRA AND EXCITONIC GROUND STATE

Figure 2 shows the evolution of several lowest electron levels as a function of increasing lateral shape anisotropy. These levels evolve from the typical case of a cylindrical quantum dot with a characteristic s, p, d,... shell structure [91] to a nanorodlike spectrum with nearly equidistant levels and no shells present. In a simplified manner, this could be understood as an evolution from a quasi-two-dimensional-like confinement effectively described by a 2D harmonic oscillator [86,91] model to a quasi-one-dimensional system described by a 1D harmonic oscillator model, so there are nearly equidistant spacings between levels.

Additionally, the lowest electron levels experience a blueshift in energy with a pronounced increase of the ground electron state energy (e_1) by 48 meV for the largest deformation considered ($t = 2$) compared with the cylindrical case ($t = 0$). This occurs despite keeping the nanostructure's volume fixed during the deformation, as mentioned above, and is due to decreased confinement in the [110] direction,

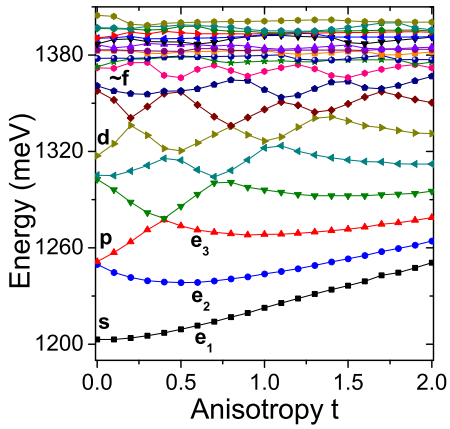

FIG. 2. Single particle electron levels as a function of nanostructure shape deformation t along the [1$\bar{1}$0] crystal axis. Lines connect levels ordered in energy. The three lowest states are marked as e_1, e_2, and e_3, respectively.

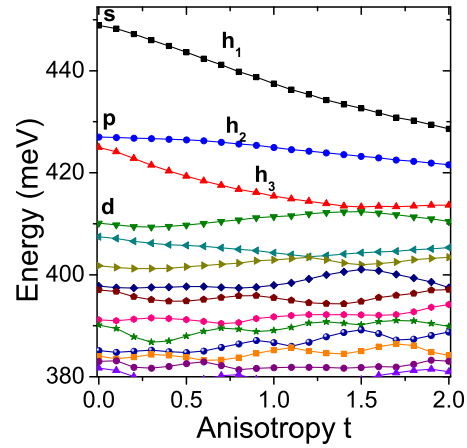

FIG. 3. Single particle hole levels as a function of nanostructure shape deformation t along the [1$\bar{1}$0] crystal axis. Lines connect levels ordered in energy. Please note the reversed ordering of hole levels with respect to electron levels. The hole ground state is marked as h_1, the first excited hole state is h_2, etc.

which is perpendicular to the direction of the nanostructure deformation direction [1$\bar{1}$0]. The f shell appears to be weakly pronounced, and there is an apparent onset of closely spaced quasicontinuum states (2D-like wetting layer states) at approximately 1380 meV. Eight lowest electrons states (16 with spin) are typically well confined within the nanostructure with the wave-function contribution in the quantum dot region varying from approximately 78% for the e_1 ground state to approximately 65% for e_8 and for $t = 0$. Higher energy states are weakly coupled at 30–45% but have a non-negligible contribution in to the nanostructure volume. Higher lying states have increasingly large content in the wetting layer and in the barrier region. The elongation further reduces localization in the dot region, which drops from 78% at $t = 0$ to 69% at $t = 2$ for e_1 and analogously for higher states.

The evolution of hole levels, which is shown in Fig. 3, is somewhat more peculiar with a complicated spectra in the elongated case, several apparent anticrossings of excited levels, and decreasing [92] energy of the ground hole h_1 level by approximately 20 meV with elongation. Various nanostructure hole states have smaller energy level spacings due to the larger effective mass of the hole. Hence, for the nonelongated case ($t = 0$), the hole p-shell splitting appears larger than that of electrons, but both splittings are in fact relatively close: 1.63 meV for electrons and 2.1 meV for holes. It should be noted that the hole d shell is apparently less separated from the excited part of the spectra than in the electron case, the f shell is practically not visible, and the confined hole shells smoothly transform into closely separated levels below approximately 385 meV. However, contrary to the electrons and again due to larger effective mass, even the excited hole states are well confined in the nanostructure with above 95–96% hole wave-function localization in the dot region for all 10 (20 with spin) lowest (h_1-h_{10}) hole states considered in the latter part of the text with respect to the excitonic calculations. Interestingly, the shape deformation has little effect on the ground hole state h_1 localization degree (reduction of an order of at most %1).

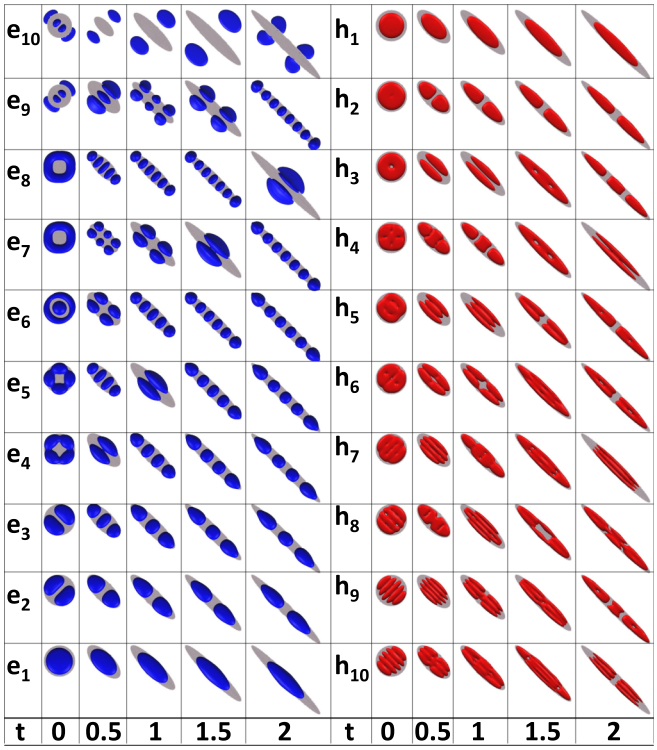

FIG. 4. Charge densities (top view) corresponding to several (10) lowest single particle electron (left) and hole (right) levels as a function of nanostructure shape deformation $t = 0, 0.5, 1, 1.5, 2$. Please note the reversed ordering of hole levels. Some of these pictures were slightly rescaled to fit the table. All isosurfaces were plotted using a constant (arbitrary) charge-density value. Gray areas mark the nanostructure region. Thus, note that some of these states are not bound within the nanostructure (e.g., e_{10} for $t = 1$). Moreover, several of these states leak profoundly into the wetting layer (e.g., e_8 for $t = 2$).

At the end of the single particle energies analysis, note that the ground and the first excited state ($s - p$) spacing decrease monotonically with deformation, dropping for electrons (Fig. 2) from 47 meV (for $t = 0.0$) to 13 meV (for $t = 2.0$) and for holes (Fig. 3) from 22 meV to 7 meV correspondingly.

Figure 4 shows charge densities corresponding to single particle levels shown in Fig. 2 and Fig. 3. For electron states, the transition from a cylindrical to a quasi-one-dimensional confinement is apparent and manifests itself in the charge density by an increasing number of nodal planes along the elongation axes. This is particularly well visible for highly-elongated cases (e.g., $t = 2$), where the manifold of the lowest electron states starts from a nodeless ground state. Then, the first excited state has one nodal plane, the second excited state has two nodal planes, and so on.

This simple intuitive picture is somewhat complicated by the presence of apparently delocalized states intruding between localized ones. This is well visible for e_8 and $t = 2$ for example. This particular state apparently originates from e_3, which is one of the cylindrical ($t = 0$) quantum dot p-shell states that evolves to a higher energy with the shape deformation due to the presence of a node in this state aligned with the longer axis of the nanostructure. Such near-delocalized states have a significant proportional of their charge density "leaking" out of the nanostructure into the InAs wetting layer and finally into the InP barrier. Another example of an interesting behavior is seen for higher excited states e_9 and e_{10} for cases of $t = 0$ and $t = 0.5$. Here, these states again have mixed character with a proportion of charge density in the nanostructure hybridized with the rest of it penetrating the wetting layer. Finally, there are electron states shown here as well (e.g., e_{10} for $t = 1.5$) with no apparent density in the quantum dash area but rather delocalized in the wetting layer.

The ground hole state charge density is shown on the right-hand side of Fig. 4 (please note again the reversed ordering of hole levels) and behaves similarly to the ground electron state. The only difference is that h_1 seems to localize more strongly within the nanostructure, whereas e_1 shows some spreading (leakage) in the ([110]) direction perpendicular to the deformation. Generally, all (10) hole states shown here are more strongly localized in the nanostructures area. This is expected since plots shown here must be consistent with the numbers discussed earlier (degrees of localization reaching 96%).

Finally, note that the excited state h_2 shows a simple behavior with a single nodal plane, but higher excited hole states have far more complicated nodal structure than electrons because they have nontrivial nodes (both in [1$\underline{1}$0] and [110] directions)—an apparent manifest of the multiband character of holes.

Apart from energies and charge densities, in the tight-binding formalism, one can naturally inspect orbital contribution from different atomic orbitals constituting single particle quantum dot confined states. The orbital contribution to the ground hole state is dominated by lateral p atomic orbitals (p_x and p_y) reaching 72–73% with a significant proportion of 24% from d orbitals (d_{yz} and d_{zx}) and much smaller contributions from other states, most notably p_z, d_{xy}, and s altogether constitute no more than 3% of the total hole ground state charge density (for more details, see the Appendix). For completeness, it should be mentioned that the ground electron state is built predominantly by s and s^* atomic orbitals (over 90% contribution) with a small 4–5% admixture of p_z orbitals and a much smaller contribution from other orbital species (p_x, p_y, and d_{xy}). Presence of p-type orbitals in the electron state or s orbitals in the ground hole state are not surprising, and it is a direct manifestation of a multiband and multivalley character of the tight-binding calculation. Moreover, despite pronounced changes of single particle state energies with the deformation, the orbital contribution is very little affected and stable with the deformation (for more details, please see Fig. 17 in the Appendix). Hence, it can be speculated that the key features of elongated system spectra are related to the overall spatial character of single particle states rather than their particular orbital components.

Quasiparticle states are next used as the input for the many-body (up to f-shell) calculation of excitonic spectra, and the resulting excitonic ground state energy evolution is shown in Fig. 5. Since we could observe the presence of different shells in the single particle spectra, it is interesting to check how these will affect the excitonic spectra. Hence, a series of configuration interaction calculations were performed with a systematically increasing number of electron

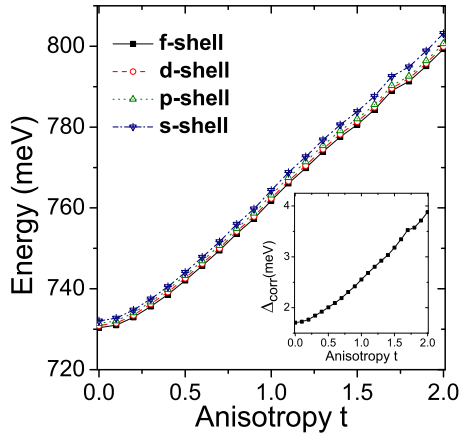

FIG. 5. Exciton ground state energy as a function of nanostructure shape deformation t along the [1$\underline{1}$0] crystal axis. Lines correspond to cases with different numbers of single-particle shells (s, p, d, and f) included in the configuration interaction calculation. Inset: the difference between ground state X energy calculated using s shell only and all shells up to f.

and hole shells accounted for, and results are summarized in Fig. 5. For the single exciton, this corresponds to 4, 36, 144, and 400 electron-hole configurations for s, p, d, and f shells, respectively. Since there is no shell structure for elongated systems and the f shell is not well pronounced even for cylindrical dot, using the notion of "shell" should not be taken literally. Accounting for the s shell means accounting for the ground electron and hole states only, p shell corresponds to the 3 (6 with spin) lowest electron and 3 (6 with spin) lowest hole states, d shell is 6 (12 with spin) states for each of the charged carriers, and f shell corresponds to accounting for 10 (20 with spin) of each of the single particle states. The energetic difference between cases accounting for s and f is shown as well (inset) in Fig. 5, and the correction due to the presence of higher shells is only approximately 1.7 meV for the $t = 0$ symmetrical case, while it reaches a more substantial 3.9 meV for the largest considered deformation. The trend shown on the inset in Fig. 5 is intuitive since one could expect a larger role of configuration mixing in the case of closely spaced levels for elongated systems of broken symmetry than in more cylindrical cases with well separated shells. However, the effect of inclusion of higher levels seems to be a small (few meV) correction compared to the overall excitonic energy of approximately 750–800 meV, but this particular difference ($s - f$) is a direct measure of the correlation effects due to the admixture of higher energy configurations and will play a crucial role (e.g., in the magnitude of excitonic complexes binding energies discussed later in the text). Finally, note that for all cases considered in Fig. 5, within small deformation ranges, the excitonic energy changes little since the decreased confinement in one direction ([110]) is compensated by the increased confinement in the other [1$\underline{1}$0] direction, which is consistent with our previous work on weakly elongated quantum dots [66] with $t \leqslant 0.2$. The ground exciton state's upward shift in energy is thus only approximately 2.6 meV for the $t = 0.2$ case with respect to the $t = 0$ system. However, for larger deformations, there is a clear almost linear growth of excitonic energy reaching approximately 800 meV for $t = 2.0$, which is approximately 69 meV larger than for the nonelongated quantum dot. It should be emphasized that the increase of excitonic ground state energy with an elongation (69 meV shift) is determined mostly by single particle energy contributions (68 meV) of electrons and holes forming an exciton. There is thus apparently only a relatively small magnitude (≈1 meV) of change of electron-hole Coulomb interaction between cylindrical and elongated cases. However, there are different contributions to electron-hole interaction due to the direct term and correction from correlations—these effects will be discussed in the latter part of the text where excitonic complexes will be discussed.

III. EXCITONIC FINE STRUCTURE: BRIGHT AND DARK EXCITONS

Apart from the main features, it is interesting to study the details of excitonic spectra, i.e., its fine structure. Typical quantum dot spectra consist of two pairs of excitonic states. One pair is formed by two states with antiparallel electron-hole spin alignments leading to an optically active bright exciton doublet. The second pair, which is energetically below the bright excitons (due to electron-hole exchange) is a doublet of two dark excitonic states with parallel electron-hole spins. Both of these doublets can be further split by various effects including the presence of anisotropic lattice, strain, and alloying [66,93]. The bright exciton splitting is also commonly known as the fine structure splitting.

Figure 6 shows energy difference between the lowest bright exciton state and the higher energy dark exciton. Notably, this splitting goes down with the elongation in all considered approximations in the configuration interaction calculation. We can understand that in terms of decreasing electron-hole exchange interaction due to the change of the lateral confinement with a progressing deformation, but we should also note that this energy difference is affected by splittings also within bright and dark doublets, which are discussed later.

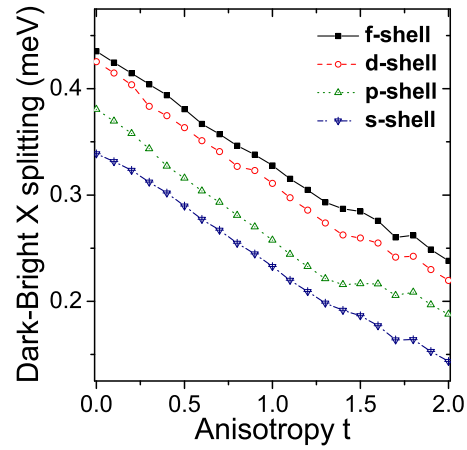

FIG. 6. The dark-bright exciton splitting (electron-hole exchange splitting) as a function of nanostructure shape deformation t along the [1$\underline{1}$0] crystal axis. Lines correspond to cases with different numbers of single-particle shells (s, p, d, and f) included in the configuration interaction calculation.

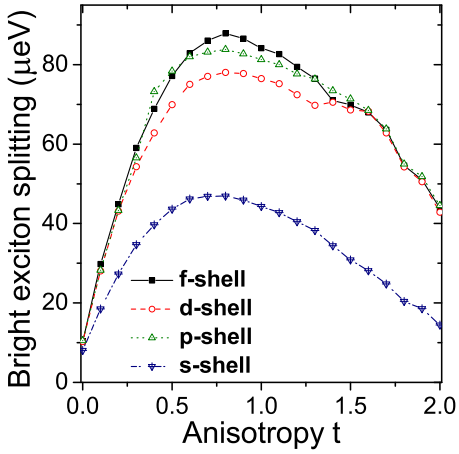

FIG. 7. The bright exciton splitting (anisotropic electron-hole exchange splitting) as a function of deformation t. Lines correspond to cases with different numbers of single-particle shells (s, p, d, and f) included in the configuration interaction calculation.

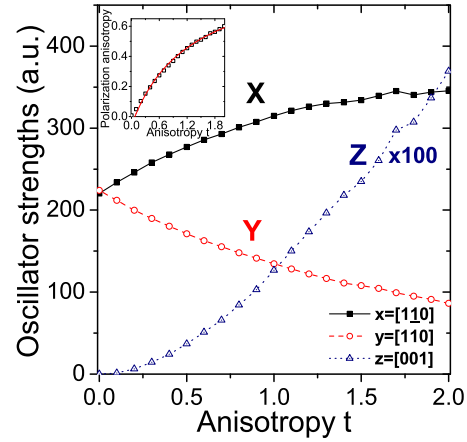

FIG. 8. The calculated excitonic optical spectrum (oscillator strengths) for the bright excitons (in-plane polarizations) and the dark exciton (out-of-plane, "z" polarization) as a function of nanostructure deformation t. The inset shows bright exciton polarization anisotropy.

Interestingly, one can also observe a non-negligible effect of higher-lying levels on dark-bright exciton energy splitting here. The difference between the d-shell and the f-shell cases is much smaller and varies between 10 to 15 μeV and is somewhat larger for elongated cases.

One could question here the convergence of the configuration interaction method with respect to the number of shells included. In fact, we will aim to address this problem in a future work, but currently accounting for shells higher than f is prohibitively numerically demanding. For the dark-bright exciton splitting, a rough estimate of such error would be approximately 30 μeV, which is still much smaller than the absolute value of the dark-bright exchange splitting.

Figure 7 shows the splitting of the bright exciton (the fine structure splitting) as a function of the deformation. One can observe two characteristic and peculiar features here. First, there is again a significant difference between configuration interaction results when accounting for different shells. A "customary" approach with s shell only reproduces well the general trend, but quite importantly it strongly underestimates the magnitude of the splitting by approximately half. The addition of higher energy configurations has little effect for weakly deformed systems, e.g., for a cylindrical case (where the fine structure splitting is present due to low lattice symmetry despite the cylindrical shape), the contribution from the s-shell is 8 μV and dominates the total splitting of 10.5 μV. However, the importance of higher levels is pronounced for elongated systems, and this can be intuitively understood since the reduced symmetry would seem to promote increased mixing between configurations. For a moderately deformed nanostructure and parameter value t between approximately 0.5 and 1.2, the fine structure splitting dependence on the number of included shells is far from trivial, e.g., the addition of d shell apparently reduces the bright exciton splitting compared to p-shell inclusion only. Interestingly, for larger deformations ($t > 1.5$), the addition of higher shells (above the p shell) has a small effect on the splitting. For the largest considered deformation, the contribution due to s shell only gives splitting of 14.4 μeV, and the addition of the p shell increases the splitting by an additional 28.5 μeV, giving the total splitting of 44.5 μeV. Further addition of d and f shells curiously decreases the splitting but only by 0.7 μeV. It thus appears that for elongated cases, most of the splitting is given by accounting for the ground, first, and second excited electron and hole levels, whereas the ground state orbitals contribute as little as 1/3 to the splitting. Moreover, our previous results demonstrate that the bright exciton splitting is also a sensitive function of overall nanostructure volume (height and length) as well as intermixing effects due to alloying in the surrounding barrier.

Apart from observations regarding the correlations due to different shells, the next key effect is the trend of fine structure evolution itself. At first, the splitting goes up quasilinearly with t following predictions based on the effective mass approximation [65] and anisotropy related mixing of quantum dot heavy-hole states. However, with the increase of deformation, this trend seems to flatten up, and it saturates with a plateau ($\approx$80 μeV) at approximately $t = 0.7$ to 0.8. More curiously, with further shape deformation, the fine structure splitting in Fig. 7 is reduced with anisotropy, which is a trend clearly contradicting simple intuition.

In order to analyze this effect further, let us focus our attention on the excitonic emission spectra. Figure 8 shows emission from two bright excitonic states in the form of two linearly polarized lines $X = [1\bar{1}0]$ and $Y = [110]$. X corresponds to lower energy bright exciton state, and Y corresponds to higher energy bright exciton state. In other words, the lower energy bright exciton state is fully X polarized, whereas the energetically higher bright excitonic state is strictly Y polarized. Due to C_{2v} symmetry, these bright states do not have a Z polarized component nor do they have "mix" polarizations with each other. More details regarding data plotted in Fig. 8 will be given in the latter part of the paper. For the $t = 0$ case, there is only a small intensity difference between these two lines due to the presence of anisotropic crystal lattice, strain, and piezoelectricity [66]. For $t > 0$, the dominant oscillator strength comes from X

polarization, which is thus followed by an elongation axis, but for the Y polarized line, the oscillator strength is reduced with elongation, with the ratio $I_{\max}/I_{\min} = I_X/I_Y$ going from ≈1 for $t = 0.0$ to over 4 for $t = 2.0$. The growth of X-polarized line oscillator strength is thus strictly followed by the decrease in Y-polarized line oscillator strength. Curiously, the $I_{\max}/I_{\min}$ dependence on elongation can be approximately described by a linear relation $I_{\max}/I_{\min} \approx 1 + 3/2 \times t$. A more established measure of polarization anisotropy is the polarization degree $C = (I_{\max} - I_{\min})/(I_{\max} + I_{\min})$ shown as black empty squares on the inset in Fig. 8. Polarization degree dependence on elongation ratio can be well described by the simple relation $C = t/(4/3 + t)$. A more accurate formula can be found by a fitting with $C = (t - 0.0725)/(1.26544 + t)$, shown as a red line on the inset in Fig. 8. Such a simple relation between polarization anisotropy and elongation suggests that there may be a single dominant factor strongly affecting the spectra.

It is often assumed [34] that structural quantum dot elongation leads to mixing of the bright exciton states $|1\rangle = |\frac{3}{2}, -\frac{1}{2}\rangle$ and $|-1\rangle = |-\frac{3}{2}, \frac{1}{2}\rangle$, where $\pm\frac{3}{2}$ corresponds to heavy-hole spin projection, and $\pm\frac{1}{2}$ are electron spin projections. Such mixing would lead to bright exciton splitting and the presence of two orthogonal lines of linear polarization. However, mixing of pure heavy-hole states seems to be insufficient to describe strong polarization anisotropy as observed here. Recently, several authors [94–97] have suggested a mechanism in which lateral anisotropy would effectively induce heavy-hole/light-hole mixing with the bright exciton states given as follows:

$$|\pm\widetilde{1}\rangle = \sqrt{1-\beta^2}\,|\pm\tfrac{3}{2}, \mp\tfrac{1}{2}\rangle + \beta\,|\mp\tfrac{1}{2}, \mp\tfrac{1}{2}\rangle. \tag{3}$$

This would effectively add-mix an exciton state heavy-hole component $|\frac{3}{2}\rangle$ with a light-hole component of opposite projection $|-\frac{1}{2}\rangle$, correspondingly mixing $|-\frac{3}{2}\rangle$ with $|\frac{1}{2}\rangle$. The two bright exciton eigenstates are then [95]

$$\begin{aligned} |\widetilde{X}\rangle &= \frac{1}{i\sqrt{2}}(|+\widetilde{1}\rangle - |-\widetilde{1}\rangle), \\ |\widetilde{Y}\rangle &= \frac{1}{\sqrt{2}}(|+\widetilde{1}\rangle + |-\widetilde{1}\rangle), \end{aligned} \tag{4}$$

where β is a measure of that mixing, and the polarization anisotropy due to mixing can be descried as [95,97]

$$C(\beta) = \frac{2\beta\sqrt{3(1-\beta^2)}}{3-2\beta^2}. \tag{5}$$

We can use a fit to the above equation in order to effectively retrieve β from our atomistic calculations of the polarization degree. The results are shown in Fig. 9, where β increases monotonically with the deformation t and reaches a considerable value of ≈0.5 for the largest considered deformation. Our previous calculations for cylindrical nanowire quantum dots [90] indicate that further increase of aspect ratio could in fact lead to the formation of a light-hole dominated exciton, but the analysis of light-hole excitons goes beyond the scope of the current work. Additionally and contrary to tall (high vertical aspect ratio) nanowire quantum dots [90], the orbital contribution of single particle states in flat (3 nm of height) nanostructure is not changed much with the deformation (for the ground hole state in particular; see the discussion earlier and the Appendix), and the large β content corresponds to a change in the envelope character of the hole wave function rather than in its microscopic part. Here, the term "envelope" was borrowed from the language of continuous media approximation (and methods such as the effective mass approach), and it should be used with great caution since the notion of the "envelope" is not present in the linear combination of atomic orbitals approach utilized by the tight-binding method.

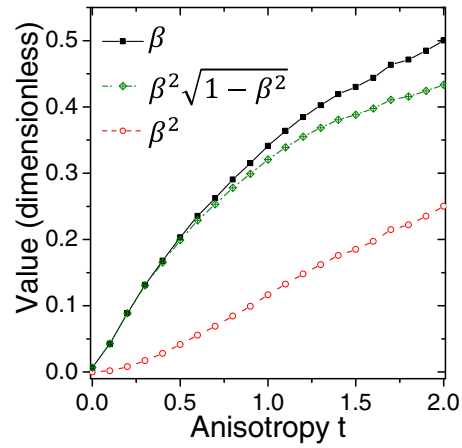

FIG. 9. Strength of light-hole/heavy-hole mixing β retrieved exciton polarization anisotropy (inset on Fig. 8) using Eq. 5. Additionally, two different functions of β are shown for the sake of discussions regarding the bright exciton splitting and dark exciton optical activity.

Let us now return to the matter of the bright exciton spectra as discussed above and shown earlier in Fig. 7. For clarity, we plot this splitting (for f-shell case only; solid-line/squares) again in Fig. 10, but this time it is compared with two simple model estimations based on recent work by Tsitsishvili [96], where the bright exciton splitting in the case of significant

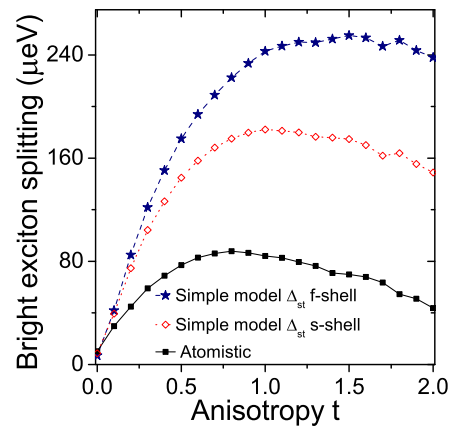

FIG. 10. Estimation of the bright exciton splitting from a phenomenological model and from atomistic calculations (black squares) as a function of nanostructure deformation t. Two simple model calculations use Δ_{ST} and β retrieved from atomistic calculation by either accounting for the electron and hole s shells only (red diamonds) or including single particle levels up to the f shell (blue stars).

light-hole admixture could be given as $\approx\frac{4}{\sqrt{3}}\beta\sqrt{1-\beta^2}\Delta_{ST}$, where Δ_{ST} is the "usual" (i.e., nonanisotropic) electron-hole exchange related to dark-bright exciton splitting shown previously in Fig. 6. The dependence $\beta\sqrt{1-\beta^2}$ term is shown in Fig. 9, where it is compared with β and β^2, and it shows sublinear dependence on t (β^2 is shown here for comparison and because it will play a role in later discussion of the dark exciton spectra). The $\beta\sqrt{1-\beta^2}$ term is then multiplied by the dark-bright exciton splitting Δ_{ST}, which gets reduced with increasing deformation (Fig. 6), as discussed earlier. Hence, for elongated systems, there are two opposing effects. The first is the increasing contribution ($\beta\sqrt{1-\beta^2}$) due to light-hole admixture that leads to the increase of the splitting. The second opposing effect is the decreasing value of the electron-hole overlap leading to a reduction of the dark-bright exciton splitting. These two effects combined together lead first to the growth of the bright exciton splitting with the deformation and then its saturation and decrease of the splitting with even further elongation. The simple model combined with input from the atomistic calculation (Δ_{ST} and β from excitonic energy and emission spectra, respectively) is thus able to qualitatively explain the behavior of the bright exciton in a highly-elongated system, but we should also emphasize it is only a qualitative agreement. Additionally, the simple model was used here with two cases, i.e., with Δ_{ST} and β retrieved from atomistic calculation by either accounting for the electron and hole s shells only (red diamonds in Fig. 10) or including single particle levels up to the f shell (blue stars in Fig. 10). In both cases, the phenomenological model overestimates the value of splitting by a large factor (up to approximately 3), especially for large t values where correlation effects increase, and the fully atomistic many-body calculation is required for the qualitative prediction of splitting magnitude. Notably, the overestimation of the bright exciton splitting is larger for the case when using apparently more accurate (i.e., f-shell) dark-bright exciton splitting taken from atomistic calculations. It was checked that β is practically identical for the s-shell and f-shell cases, so the difference lies in Δ_{ST}, and since the phenomenological model was developed without accounting for correlation effects, thus configuration mixing seems to be the main source of discrepancy between the phenomenological model and exact diagonalization calculations.

Based on the above, one can conclude that the strong admixture of the light-hole component could explain polarization properties of the bright excitons and their splitting in strongly elongated systems; moreover, it turns out that light-hole admixture would also have a pronounced effect on the dark exciton properties. Our calculations indicate that with an increasing deformation, one of the dark excitons has a non-negligible oscillator strength [shown in Fig. 8 as the z (out-of-plane) polarized line] with magnitude reaching considerable proportion (approximately 1%) of the X-polarized bright exciton emission. This dark exciton nonzero optical activity comes from the higher energy dark exciton state, where the other (low energy) state remains fully dark, which is consistent with group-theoretical predictions for heavy-hole dominant C_{2v} quantum dots [42,43]. It should be noted however that such large dark exciton optical activity is orders of magnitude stronger than that observed for weakly deformed quantum dots [66,98]. In a phenomenological model accounting for the light-hole exciton admixture to the dark exciton state [94,96], the magnitude of the dark exciton activity should follow β^2 dependence [94]. This is in fact qualitatively consistent with our results, i.e., with the z-polarized line in Fig. 8 and β^2 in Fig. 9 showing the same qualitative behavior. We note here that such pronounced optical activity of the dark exciton could have potential applications in quantum information and computation [51–53] since the dark state is both long-lived and optically addressable at the same time, and its properties could likely be tailored by the degree of nanostructure elongation.

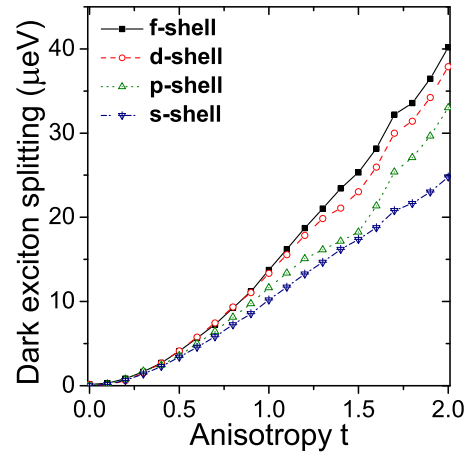

FIG. 11. The dark exciton splitting as a function of deformation t. Lines correspond to cases with different numbers of single-particle shells (s, p, d, and f) included in the configuration interaction calculation.

Apart from the optical activity, it is instructive to study the dark exciton splitting as shown in Fig. 11. The dark exciton splitting goes from a small value of 0.14 μeV for a cylindrical $t = 0$ system to a substantial splitting exceeding 40 μeV for $t = 2.0$. One should note that this is an extraordinarily large dark exciton splitting, comparable with that of the bright exciton. Based on a simple model [96], one can expect the dark exciton splitting to grow proportionally to β (and thus to t) due to the light-hole exciton admixture to the dark exciton $|\pm 2\rangle$ state. Therefore, a substantial content of the light-hole exciton will have a dramatic impact on the dark exciton properties, including the dark exciton splitting. One can however observe yet another effect that cannot be easily captured even qualitatively by a simple model. Namely, for deformations t larger than 0.5, one can notice an increasing role of higher-lying shells, with the magnitude of dark exciton splitting increasing progressively with the admixture of these shells. This leads to a general trend of the dark exciton emission resembling more quadraticlike behavior as a function of t with f shell included and more linearlike for the s shell included only.

To summarize this section, note that the calculated range of the bright exciton splittings (from 10 to 88 μeV) falls reasonably well within the range of values observed experimentally [56] for large-aspect ratio quantum dashes emitting at approximately 800 meV (i.e., from approximately 25 to nearly 200 μeV). However, we emphasize that in this work we do not aim at a direct comparison with a particular quantum dash

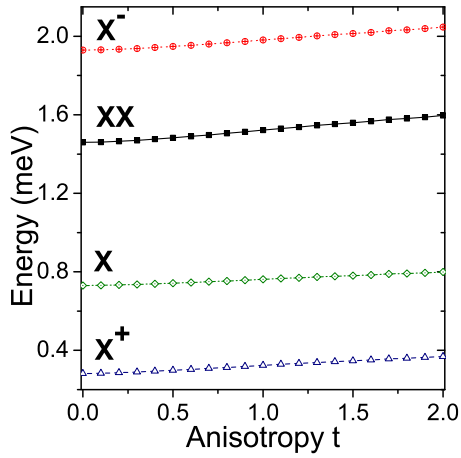

FIG. 12. Ground state energy evolution for the biexciton (XX), exciton (X), and positively (X^+) and negatively (X^-) charged trions as a function of nanostructure deformation t.

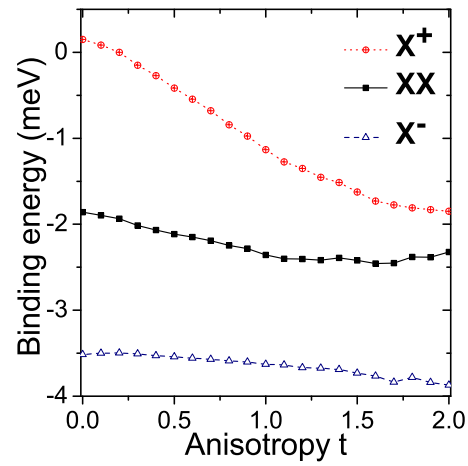

FIG. 13. Binding energies of the biexciton (XX) and positively (X^+) and negatively (X^-) charged trions as a function of nanostructure deformation t.

or quantum dot experiment but rather focus on the analysis of general trends with shape elongation. Moreover, a detailed comparison with a particular experiment [56] should include a comprehensive knowledge of nanostructure morphology, which is often near impossible to obtain [17,18,21,59]. Nevertheless, one can argue here that obtained results strongly suggest that it is unlikely for [1$\underline{1}$0] elongated quantum dashes to achieve a very small fine structure splitting unless other phenomena such as alloying due to annealing or composition intermixing are included into the consideration [27,40], external fields are applied [32], or different growth modes are considered (as discussed in the following section). Otherwise, nanostructure designers should typically aim for nonelongated [13] or weakly [110] elongated nanostructures, where small elongation along the [110] axis [66] should lead to reduced fine structure splitting by minimizing the anisotropic contribution due to strain. On the other hand, the profoundly increased dark exciton state optical activity in highly-elongated systems could in principle open new routes for quantum dash applications, including entanglement generation via the time-bin approach [54,55] or utilizing the dark exciton as an optically addressable quantum bit [51–53,99].

IV. EXCITONIC COMPLEXES

Besides considering a single exciton, it is instructive to study spectral properties of excitonic complexes, i.e., positively (X^+) and negatively (X^-) charged excitons and the biexciton (XX). From here on, the results of calculations will be shown only for the case with the wetting layer included in the calculation. Understanding of the biexciton spectra is particularly relevant from an application point of view since in various schemes [7,55] its plays an essential role in entanglement generation.

The ground state energies of these complexes are presented in Fig. 12, and they show a weak monotonically increasing trend with t similar to that of the single exciton (X) shown previously in Fig. 5 and presented here as well for the purpose of comparison. Contrary to a single exciton, in an optical experiment, it is not straightforward to measure ground state energies directly, so one must consider transition energies. Therefore, Fig. 13 shows the evolution of binding energies of X^+, X^-, and XX as a function of shape deformation t. Similarly to a photoluminescence experiment, these binding energies were calculated with respect to the single exciton. For the case of XX, this means the optical recombination leaving X as a final state. The energy of this bright optical transition (i.e., $E_{XX} - E_X$) is then compared with that of the bright exciton E_X to define the binding energy of a complex. The binding energy thus measures the energetic difference between bright lines from recombining XX, X^+, X^- complexes and the lowest bright X state.

Depending on the nature of a complex, the binding energy spectra reveal a different behavior, with XX and X^- showing only a weak change with shape elongation. The XX binding energy varies from approximately -1.9 to approximately -2.5 meV, similar to our earlier results [56] obtained for quantum dashes with triangular cross sections. Alternatively, X^- is more bound with the binding energy changing from -3.5 to nearly -3.9 meV for the largest considered deformation. Here, we utilize a convention in which a negatively bound complex has emission energy lower than the bright single exciton state.

The positively charged exciton X^+ shows a much more pronounced trend with the shape elongation. Its binding energy goes from a small positive value of 0.15 meV for a cylindrical system to almost -1.8 meV for $t = 2.0$. It is interesting to analyze such different behaviors of X^+, and since XX and X^+ differ by the presence of an additional hole, one can speculate that the difference between all these excitonic species is related to the hole state properties.

More formally, one can estimate these binding energies in terms of Coulomb integrals calculated for an electron and a hole in their ground states e_1 and h_1, respectively: [57,100,101]

$$\begin{aligned}\Delta E(XX) &= J_{e1e1} + J_{h1h1} - 2J_{e1h1} + \Delta_{\text{corr}}(XX - X)\\ \Delta E(X^-) &= J_{e1e1} - J_{e1h1} + \Delta_{\text{corr}}(X^- - e)\\ \Delta E(X^+) &= J_{h1h1} - J_{e1h1} + \Delta_{\text{corr}}(X^+ - h),\end{aligned} \tag{6}$$

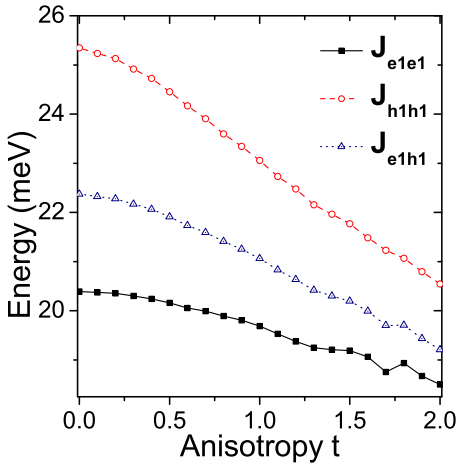

FIG. 14. Electron-electron (J_{e1e1}), electron-hole (J_{e1h1}), and hole-hole (J_{h1h1}) direct Coulomb integrals calculated for electrons and holes occupying their ground states (e_1 and h_1, respectively) as a function of nanostructure deformation t. Please note the same sign convention used for all these terms.

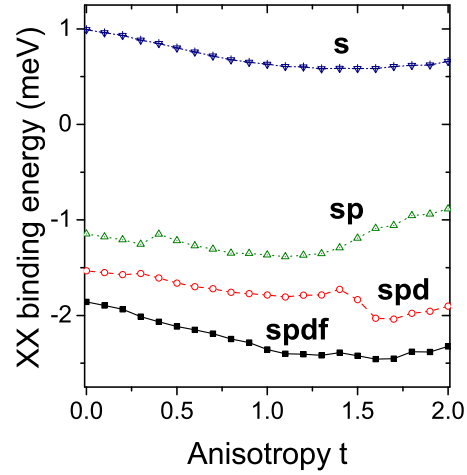

FIG. 15. Evolution of the biexciton binding energy as a function of nanostructure deformation t and the number of single particle shells included in the configuration interaction calculation.

where J are electron-electron, hole-hole, and electron-hole Coulomb integrals mentioned above. Δ_{corr} are (negative) corrections due to correlation (and exchange) effects and are accounted for by the exact diagonalization (configuration interaction). Similarly to experiments [56], the recombination process happens between the initial (e.g., XX) and a final (e.g., X) state of two different excitonic complexes. The above formula should in principle help us to understand properties of excitonic complexes in terms of contributions from selected Coulomb integrals, which are shown in Fig. 14.

The hole-hole repulsion is reduced by approximately 5 meV with the anisotropy, whereas the electron-electron repulsion is reduced by a 1.9 meV factor only, and the electron-hole attraction shows an intermediate trend [the sign of J_{e1h1} was set as positive according to the convention used in Eq. (6)]. The pronounced change of an integral involving a hole state suggests that the hole is apparently more prone to the reduction of lateral confinement (shrinking) in the [110] direction, perpendicular to the shape elongation in [1$\underline{1}$0]. Although likely oversimplified, this is consistent with charge density plots shown earlier in Fig. 4, where h_1 seems to be more localized in the nanostructure for elongated cases, whereas e_1 tends to leak out, partially overcoming the effect of elongation.

The strongly decreasing value of the J_{h1h1} integral combined with $\Delta E(X^+)$ from Eq. (6) seems to be able to qualitatively explain the strong X^+ evolution with deformation as well as weak changes of the X^- and XX states. However, the simple estimations based solely on the ground state properties are not able to address the overall binding energy of excitonic complexes. This is well illustrated in Fig. 15, where the XX binding energy was calculated by using different numbers of electron and hole levels accounted for in the configuration interaction calculation. The s-shell calculation effectively corresponds to Eq. (6) with correction due to correlations $\Delta_{\text{corr}}(XX - X)$ set to zero, whereas the overall trend with the deformation does not change strongly between different approaches, only inclusion of s, p, d, and f shells seems to produce binding energies reaching -2.5 meV in a reasonable agreement with the experiment [56,64].

For the case including the f shell, the correction to the XX binding energy due to correlations $\Delta_{\text{corr}}(XX - X)$ is approximately -3 meV for all considered t values. However, it should be emphasized again that the correction due to correlations $[\Delta_{\text{corr}}(XX - X)]$ in the XX binding energy in the recombination process is affected by both the correlations in the initial XX state $[\Delta_{\text{corr}}(XX)]$ and the final X states $[\Delta_{\text{corr}}(X)]$. Correlations in the initial state, i.e., in the XX ground state (Fig. 16), shift the energy down by 5.4 meV for $t = 0$ as compared to a single electron-hole s-shell configuration. This correction grows with deformation and reaches a substantial 10 meV for $t = 2.0$. A pronounced ground XX state energy shift due to configuration mixing is also well known in standard nonelongated quantum dots [91] and is a key factor determining XX binding energy in the emission spectra. However, the magnitude of this correction reaching

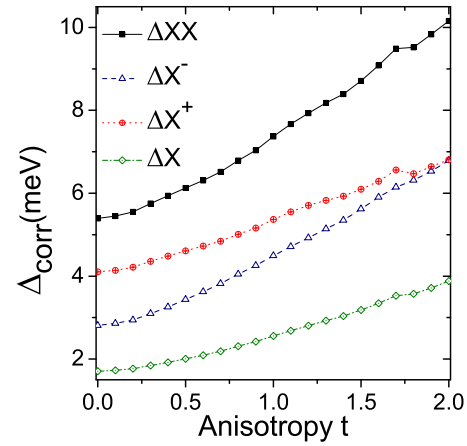

FIG. 16. Correction due to configurations mixing for the biexciton (XX), exciton (X), and positively (X^+) and negatively (X^-) charged trions as a function of nanostructure deformation t.

10 meV is far larger than in typical self-assembled quantum dots. Moreover, here, differently from cylindrical systems, the correlation correction is also present and non-negligible in the final single exciton state. This effect was briefly mentioned earlier in this paper (inset in Fig. 5) with the correlation correction reaching the considerable value of -3.9 meV for a single exciton in its ground state and $t = 2.0$. In elongated systems, correlations thus have a strong effect on both XX (initial) and X (final) states, and in both of these excitonic species, these corrections increase their magnitudes with the deformation. However, in the XX recombination spectra case, these terms effectively partially cancel out, leading to apparently stable biexciton binding energy with elongation. Finally, we speculate that the addition of higher excited electron and hole levels (currently prohibited by numerical complexity) would likely further reduce the XX binding energy closer to the experimentally observable values, i.e., approximately -3 meV.

V. SUMMARY

An increasing nanostructure shape anisotropy leads to the transition from a cylindrical quantum dot to a heavily-elongated quantum dash. In this work, this transition was shown to have a strong impact on both the single particle and many-body properties of such systems. As expected, the shape deformation leads to an increasing splitting of the bright exciton, but at a certain aspect ratio, the splitting saturates and peculiarly it is reduced with further elongation. The emission from the bright exciton is characterized as well by a strong degree of polarization anisotropy. The magnitudes of fine structure splitting (40–90 μeV) as well as the polarization degree of up to 0.6 obtained here by atomistic calculations compare well with experimental data for InAs/InP quantum dashes, even though we did not focus on alloying (mixed composition) effects, which are always present in epitaxial systems. The main spectral features of strongly elongated systems can also be qualitatively explained in terms of a simple model assuming anisotropy induced contribution of a light-hole exciton to a heavy-hole dominated excitonic ground state. This contribution affects the dark excitonic states as well, leading to a dark exciton splitting growing proportionally with the shape deformation and the magnitude of splitting reaching comparable values to that of the bright exciton. Moreover, the dark exciton gains a very significant increase of its optical activity, reaching approximately 1% of the dominant bright exciton line. The shape elongation was further found to have a strong impact on correlation effects in these nanostructures. The admixture of higher excited (often with tails in the wetting layer) electron and hole states (up to the tenth level corresponding to the f shell of a cylindrical quantum dot) has a pronounced effect on the ground excitonic complexes states, magnitudes of dark and bright excitons splitting of the single exciton, and binding energies of excitonic complexes. Finally, this paper showed that the control of the degree of elongation (or quantum dot anisotropy) could in principle be used to tailor optical properties of nanostructures in a broad range of values, including cases with a curiously strong optical activity of the dark exciton.

ACKNOWLEDGMENTS

The author would like to thank M. Gawełczyk, K. Gawarecki, and G. Sęk for insightful discussions. The support from the Polish National Science Centre based on Decision No. 2015/18/E/ST3/00583 is kindly acknowledged.

APPENDIX: ORBITAL CONTRIBUTIONS

Since the ground hole single particle state has a dominant contribution to several lowest exciton states (two dark and two bright) and due to the importance of heavy-hole/light-hole couplings as discussed above, let us inspect atomic orbital coefficients in the tight-binding expansion (linear combination of atomic orbitals) of the ground hole state wave function shown in Fig. 17 (left). One should analyze such plots as in Fig. 17 with care and note first that apart from atomic orbital contribution, there is a strong "envelope" contribution that is not straightforward to retrieve from the tight-binding method and is not shown in Fig. 17. Nonetheless, inspection of Fig. 17 reveals that contributions from p_x and p_y orbitals (sum of squared moduli) are the same and only weakly depend on the deformations. The combined contribution of lateral p orbitals reaches 72–73% and orbitalwise is a dominant contribution to the wave function. Moreover, one can see the important contribution of approximately 24% combined from the d_{yz} and d_{zx} orbitals, which again does not change with the deformation. However, the elongation affects the p_z orbital's contribution, which goes from approximately 1.3% for $t = 0$ to almost 2.7% for $t = 2.0$. Contributions from s (and s^*) are (not surprisingly) much smaller and do not exceed 1% [inset on Fig. 17 (left)]. Here, z corresponds to the [001] direction, and it must be strongly emphasized that the x and y indices refer to crystal axes [100] and [010], respectively, and not to the nanostructure elongation axes $X = [1\underline{1}0]$ and $Y = [110]$. Since [100] and [010] are equivalent (whereas $X = [1\underline{1}0]$ and $Y = [110]$ are not), p_x and p_y contributions must be identical.

The reason for presenting Fig. 17 is twofold. First, in simplified models and contrary to atomistic approaches, one very often neglects contributions to the ground hole state other than from the p_x and p_y orbitals. Such an approach is apparently doubtful here since the contribution from d orbitals reaches a significant 1/4 of the entire hole-function charge density. Secondly, analysis of only selected

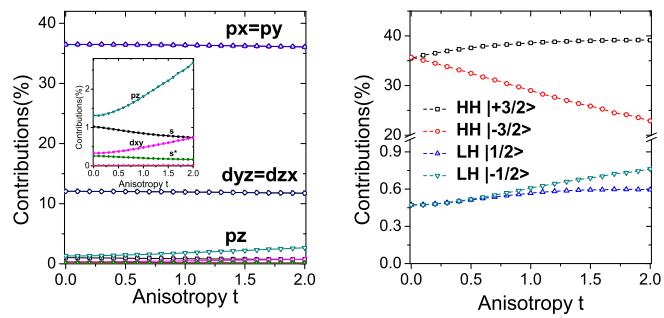

FIG. 17. Atomic orbital contributions (left) and combination of atomic orbital constituting light-hole (LH) and heavy-hole (HH)-like combinations as a function of nanostructure deformation t.

components can be somewhat misleading. This is emphasized in Fig. 17 (right), where p atomic orbitals were combined to form "atomic" heavy-hole and light-hole combinations [e.g., $|\frac{3}{2}\rangle = \frac{1}{\sqrt{2}}(|p_x^{\uparrow}\rangle + i|p_y^{\uparrow}\rangle)$], and the sum of their squared moduli over all atoms in the system is plotted as a function of shape elongation t. $|\pm\frac{3}{2}\rangle$ clearly varies with elongation, whereas the separated square moduli of p_x and p_y do not. This reveals an apparent change of phases between p_x and p_y atomic orbitals that was simply not visible in straightforward $|p_{x,y}|^2$ plots. Next, the p_z contribution grows with deformation, yet it is present (1%) even for a cylindrical case, which is contrary to assumptions made by simplified approaches. Moreover, the p_z orbital or the light-hole "atomic" component [constructed from atomic p_x, p_y, and p_z orbitals shown in Fig. 17 (right)] reveals only a weak trend with elongation. Thus, the analysis of p_z orbitals or light-hole "atomic" components only and the neglect of the overall wave-function character (i.e., spatial charge density distribution) are not sufficient by themselves to explain the increase of dark exciton optical activity by nearly four orders of magnitude.

[1] R. Anufriev, J.-B. Barakat, G. Patriarche, X. Letartre, C. Bru-Chevallier, J.-C. Harmand, M. Gendry, and N. Chauvin, Nanotechnology **26**, 395701 (2015).

[2] J. Yuan, H. Wang, R. P. van Veldhoven, J. Wang, T. de Vries, B. Smalbrugge, C. Jin, P. Nouwens, E. J. Geluk, A. Y. Silov *et al.*, Appl. Phys. Lett. **98**, 201904 (2011).

[3] M. Benyoucef, M. Yacob, J. Reithmaier, J. Kettler, and P. Michler, Appl. Phys. Lett. **103**, 162101 (2013).

[4] A. Kors, K. Fuchs, M. Yacob, J. Reithmaier, and M. Benyoucef, Appl. Phys. Lett. **110**, 031101 (2017).

[5] P. Michler, A. Kiraz, C. Becher, W. V. Schoenfeld, P. M. Petroff, L. Zhang, E. Hu, and A. Imamoglu, Science **290**, 2282 (2000).

[6] C. Santori, M. Pelton, G. Solomon, Y. Dale, and Y. Yamamoto, Phys. Rev. Lett. **86**, 1502 (2001).

[7] O. Benson, C. Santori, M. Pelton, and Y. Yamamoto, Phys. Rev. Lett. **84**, 2513 (2000).

[8] R. M. Stevenson, R. J. Young, P. Atkinson, K. Cooper, D. A. Ritchie, and A. J. Shields, Nature (London) **439**, 179 (2006).

[9] E. Knill, R. Laflamme, and G. J. Milburn, Nature (London) **409**, 46 EP (2001).

[10] E. Waks, K. Inoue, C. Santori, D. Fattal, J. Vuckovic, G. S. Solomon, and Y. Yamamoto, Nature (London) **420**, 762 (2002).

[11] P. Kok, W. J. Munro, K. Nemoto, T. C. Ralph, J. P. Dowling, and G. J. Milburn, Rev. Mod. Phys. **79**, 135 (2007).

[12] R. Williams, G. Aers, P. Poole, J. Lefebvre, D. Chithrani, and B. Lamontagne, J. Cryst. Growth **223**, 321 (2001).

[13] A. Kors, J. P. Reithmaier, and M. Benyoucef, Appl. Phys. Lett. **112**, 172102 (2018).

[14] D. Dalacu, A. Kam, D. G. Austing, X. Wu, J. Lapointe, G. C. Aers, and P. J. Poole, Nanotechnology **20**, 395602 (2009).

[15] M. A. M. Versteegh, M. E. Reimer, K. D. Jöns, D. Dalacu, P. J. Poole, A. Gulinatti, A. Giudice, and V. Zwiller, Nat. Commun. **5**, 5298 (2014).

[16] M. Bouwes Bavinck, M. Zieliński, B. J. Witek, T. Zehender, E. P. A. M. Bakkers, and V. Zwiller, Nano Lett. **12**, 6206 (2012).

[17] H. Dery, E. Benisty, A. Epstein, R. Alizon, V. Mikhelashvili, G. Eisenstein, R. Schwertberger, D. Gold, J. Reithmaier, and A. Forchel, J. Appl. Phys. **95**, 6103 (2004).

[18] A. Sauerwald, T. Kümmell, G. Bacher, A. Somers, R. Schwertberger, J. Reithmaier, and A. Forchel, Appl. Phys. Lett. **86**, 253112 (2005).

[19] J. P. Reithmaier, A. Somers, S. Deubert, R. Schwertberger, W. Kaiser, A. Forchel, M. Calligaro, P. Resneau, O. Parillaud, S. Bansropun, M. Krakowski, R. Alizon, D. Hadass, A. Bilenca, H. Dery, V. Mikhelashvili, G. Eisenstein, M. Gioannini, I. Montrosset, T. W. Berg, M. van der Poel, J. Mørk, and B. Tromborg, J. Phys. D **38**, 2088 (2005).

[20] J. P. Reithmaier, G. Eisenstein, and A. Forchel, Proc. IEEE **95**, 1779 (2007).

[21] M. Z. M. Khan, T. K. Ng, and B. S. Ooi, Prog. Quantum Electron. **38**, 237 (2014).

[22] A. Musiał, P. Kaczmarkiewicz, G. Sęk, P. Podemski, P. Machnikowski, J. Misiewicz, S. Hein, S. Höfling, and A. Forchel, Phys. Rev. B **85**, 035314 (2012).

[23] A. Musiał, P. Gold, J. Andrzejewski, A. Löffler, J. Misiewicz, S. Höfling, A. Forchel, M. Kamp, G. Sęk, and S. Reitzenstein, Phys. Rev. B **90**, 045430 (2014).

[24] M. Gawełczyk, M. Syperek, A. Maryński, P. Mrowiński, Ł. Dusanowski, K. Gawarecki, J. Misiewicz, A. Somers, J. Reithmaier, S. Höfling, G. Sęk *et al.*, Phys. Rev. B **96**, 245425 (2017).

[25] Ł. Dusanowski, P. Mrowiński, M. Syperek, J. Misiewicz, A. Somers, S. Höfling, J. Reithmaier, and G. Sęk, Appl. Phys. Lett. **111**, 253106 (2017).

[26] Ł. Dusanowski, A. Musiał, A. Maryński, P. Mrowiński, J. Andrzejewski, P. Machnikowski, J. Misiewicz, A. Somers, S. Höfling, J. P. Reithmaier, G. Sęk *et al.*, Phys. Rev. B **90**, 125424 (2014).

[27] D. Jung, D. J. Ironside, S. R. Bank, A. C. Gossard, and J. E. Bowers, J. Appl. Phys. **123**, 205302 (2018).

[28] S. Azouigui, B. Dagens, F. Lelarge, J.-G. Provost, D. Make, O. Le Gouezigou, A. Accard, A. Martinez, K. Merghem, F. Grillot *et al.*, IEEE J. Sel. Top. Quantum Electron. **15**, 764 (2009).

[29] Ł. Dusanowski, M. Syperek, W. Rudno-Rudziński, P. Mrowiński, G. Sęk, J. Misiewicz, A. Somers, J. Reithmaier, S. Höfling, and A. Forchel, Appl. Phys. Lett. **103**, 253113 (2013).

[30] Ł. Dusanowski, M. Syperek, P. Mrowiński, W. Rudno-Rudziński, J. Misiewicz, A. Somers, S. Höfling, M. Kamp, J. Reithmaier, and G. Sęk, Appl. Phys. Lett. **105**, 021909 (2014).

[31] P. Mrowiński, M. Emmerling, C. Schneider, J. P. Reithmaier, J. Misiewicz, S. Höfling, and G. Sęk, Phys. Rev. B **97**, 165427 (2018).

[32] P. Mrowiński, A. Musiał, A. Maryński, M. Syperek, J. Misiewicz, A. Somers, J. Reithmaier, S. Höfling, and G. Sęk, Appl. Phys. Lett. **106**, 053114 (2015).

[33] D. Gammon, E. S. Snow, B. V. Shanabrook, D. S. Katzer, and D. Park, Phys. Rev. Lett. **76**, 3005 (1996).

[34] M. Bayer, G. Ortner, O. Stern, A. Kuther, A. A. Gorbunov, A. Forchel, P. Hawrylak, S. Fafard, K. Hinzer, T. L. Reinecke, S. N. Walck, J. P. Reithmaier, F. Klopf, and F. Schäfer, Phys. Rev. B **65**, 195315 (2002).
[35] T. Takagahara, Phys. Rev. B **62**, 16840 (2000).
[36] W. Langbein, P. Borri, U. Woggon, V. Stavarache, D. Reuter, and A. D. Wieck, Phys. Rev. B **69**, 161301(R) (2004).
[37] R. J. Young, R. M. Stevenson, A. J. Shields, P. Atkinson, K. Cooper, D. A. Ritchie, K. M. Groom, A. I. Tartakovskii, and M. S. Skolnick, Phys. Rev. B **72**, 113305 (2005).
[38] N. Akopian, N. H. Lindner, E. Poem, Y. Berlatzky, J. Avron, D. Gershoni, B. D. Gerardot, and P. M. Petroff, Phys. Rev. Lett. **96**, 130501 (2006).
[39] R. Hafenbrak, S. Ulrich, P. Michler, L. Wang, A. Rastelli, and O. Schmidt, New J. Phys. **9**, 315 (2007).
[40] F. Olbrich, J. Höschele, M. Müller, J. Kettler, S. Luca Portalupi, M. Paul, M. Jetter, and P. Michler, Appl. Phys. Lett. **111**, 133106 (2017).
[41] R. Singh and G. Bester, Phys. Rev. Lett. **103**, 063601 (2009).
[42] K. F. Karlsson, M. A. Dupertuis, D. Y. Oberli, E. Pelucchi, A. Rudra, P. O. Holtz, and E. Kapon, Phys. Rev. B **81**, 161307(R) (2010).
[43] M. A. Dupertuis, K. F. Karlsson, D. Y. Oberli, E. Pelucchi, A. Rudra, P. O. Holtz, and E. Kapon, Phys. Rev. Lett. **107**, 127403 (2011).
[44] K. Kowalik, O. Krebs, A. Lemaitre, S. Laurent, P. Senellart, P. Voisin, and J. Gaj, Appl. Phys. Lett. **86**, 041907 (2005).
[45] A. Bennett, M. Pooley, R. Stevenson, M. Ward, R. Patel, A. B. de La Giroday, N. Sköld, I. Farrer, C. Nicoll, D. Ritchie *et al.*, Nat. Phys. **6**, 947 (2010).
[46] R. M. Stevenson, R. J. Young, P. See, D. G. Gevaux, K. Cooper, P. Atkinson, I. Farrer, D. A. Ritchie, and A. J. Shields, Phys. Rev. B **73**, 033306 (2006).
[47] B. Gerardot, S. Seidl, P. Dalgarno, R. J. Warburton, D. Granados, J. Garcia, K. Kowalik, O. Krebs, K. Karrai, A. Badolato *et al.*, Appl. Phys. Lett. **90**, 041101 (2007).
[48] S. Seidl, M. Kroner, A. Högele, K. Karrai, R. J. Warburton, A. Badolato, and P. M. Petroff, Appl. Phys. Lett. **88**, 203113 (2006).
[49] F. Ding, R. Singh, J. D. Plumhof, T. Zander, V. Křápek, Y. H. Chen, M. Benyoucef, V. Zwiller, K. Dörr, G. Bester, A. Rastelli, and O. G. Schmidt *et al.*, Phys. Rev. Lett. **104**, 067405 (2010).
[50] R. Trotta, E. Zallo, C. Ortix, P. Atkinson, J. D. Plumhof, J. Van den Brink, A. Rastelli, and O. G. Schmidt, Phys. Rev. Lett. **109**, 147401 (2012).
[51] I. Schwartz, D. Cogan, E. R. Schmidgall, L. Gantz, Y. Don, M. Zieliński, and D. Gershoni, Phys. Rev. B **92**, 201201(R) (2015).
[52] I. Schwartz, E. R. Schmidgall, L. Gantz, D. Cogan, E. Bordo, Y. Don, M. Zielinski, and D. Gershoni, Phys. Rev. X **5**, 011009 (2015).
[53] M. Zieliński, Y. Don, and D. Gershoni, Phys. Rev. B **91**, 085403 (2015).
[54] C. Simon and J.-P. Poizat, Phys. Rev. Lett. **94**, 030502 (2005).
[55] G. Weihs, T. Huber, and A. Predojević, in *Quantum Dots for Quantum Information Technologies* (Springer, Cham, 2017), pp. 267–284.
[56] P. Mrowiński, M. Zieliński, M. Świderski, J. Misiewicz, A. Somers, J. P. Reithmaier, S. Höfling, and G. Sęk, Phys. Rev. B **94**, 115434 (2016).
[57] M. Zieliński, K. Gołasa, M. R. Molas, M. Goryca, T. Kazimierczuk, T. Smoleński, A. Golnik, P. Kossacki, A. A. L. Nicolet, M. Potemski, Z. R. Wasilewski, and A. Babiński, Phys. Rev. B **91**, 085303 (2015).
[58] A. Maryński, G. Sęk, A. Musiał, J. Andrzejewski, J. Misiewicz, C. Gilfert, J. Reithmaier, A. Capua, O. Karni, D. Gready *et al.*, J. Appl. Phys. **114**, 094306 (2013).
[59] V. Mlinar, M. Bozkurt, J. M. Ulloa, M. Ediger, G. Bester, A. Badolato, P. M. Koenraad, R. J. Warburton, and A. Zunger, Phys. Rev. B **80**, 165425 (2009).
[60] C. Salter, R. Stevenson, I. Farrer, C. Nicoll, D. Ritchie, and A. Shields, Nature (London) **465**, 594 (2010).
[61] C. Santori, D. Fattal, J. Vučković, G. S. Solomon, and Y. Yamamoto, Nature (London) **419**, 594 (2002).
[62] J. M. Gérard, B. Sermage, B. Gayral, B. Legrand, E. Costard, and V. Thierry-Mieg, Phys. Rev. Lett. **81**, 1110 (1998).
[63] E. Peter, P. Senellart, D. Martrou, A. Lemaître, J. Hours, J. M. Gérard, and J. Bloch, Phys. Rev. Lett. **95**, 067401 (2005).
[64] P. Mrowiński, K. Tarnowski, J. Olszewski, A. Somers, M. Kamp, J. P. Reithmaier, W. Urbańczyk, J. Misiewicz, P. Machnikowski, and G. Sęk, J. Appl. Phys. **120**, 074303 (2016).
[65] E. Kadantsev and P. Hawrylak, Phys. Rev. B **81**, 045311 (2010).
[66] M. Zieliński, Phys. Rev. B **88**, 155319 (2013).
[67] W. Rudno-Rudziński, R. Kudrawiec, P. Podemski, G. Sęk, J. Misiewicz, A. Somers, R. Schwertberger, J. Reithmaier, and A. Forchel, Appl. Phys. Lett. **89**, 031908 (2006).
[68] P. N. Keating, Phys. Rev. **145**, 637 (1966).
[69] R. M. Martin, Phys. Rev. B **1**, 4005 (1970).
[70] W. Jaskólski, M. Zieliński, G. W. Bryant, and J. Aizpurua, Phys. Rev. B **74**, 195339 (2006).
[71] C. Pryor, J. Kim, L. W. Wang, A. J. Williamson, and A. Zunger, J. Appl. Phys. **83**, 2548 (1998).
[72] T. Saito and Y. Arakawa, Physica E **15**, 169 (2002).
[73] M. Zieliński, M. Korkusinski, and P. Hawrylak, Phys. Rev. B **81**, 085301 (2010).
[74] M. Zieliński, Phys. Rev. B **86**, 115424 (2012).
[75] M. Zieliński, J. Phys.: Condens. Matter **25**, 465301 (2013).
[76] G. Bester, X. Wu, D. Vanderbilt, and A. Zunger, Phys. Rev. Lett. **96**, 187602 (2006).
[77] G. Bester, A. Zunger, X. Wu, and D. Vanderbilt, Phys. Rev. B **74**, 081305(R) (2006).
[78] A. Beya-Wakata, P.-Y. Prodhomme, and G. Bester, Phys. Rev. B **84**, 195207 (2011).
[79] G. Tse, J. Pal, U. Monteverde, R. Garg, V. Haxha, M. Migliorato, and S. Tomić, J. Appl. Phys. **114**, 073515 (2013).
[80] M. A. Caro, S. Schulz, and E. P. O'Reilly, Phys. Rev. B **91**, 075203 (2015).
[81] Piezoelectric coefficients from Ref. [78] were used. Second-order piezoelectric coefficients may somewhat vary between different authors [78,80], but contrary to highly-stressed quantum dots [102] and due to low 3% strain in InAs/InP systems and flat disk-shape geometry with little shear strains, piezoelectricity plays a negligible role here and its effect can safely be neglected for both linear and quadratic contributions.

Nevertheless, the piezoelectric potential has been accounted for in order to maintain methodological completeness.
[82] D. J. Chadi, Phys. Rev. B **16**, 790 (1977).
[83] J.-M. Jancu, R. Scholz, F. Beltram, and F. Bassani, Phys. Rev. B **57**, 6493 (1998).
[84] S. Lee, F. Oyafuso, P. von Allmen, and G. Klimeck, Phys. Rev. B **69**, 045316 (2004).
[85] M. Zieliński, Acta Phys. Pol. A **122**, 312 (2012).
[86] P. Michler (ed.), *Topics in Applied Physics* (Springer, New York, 2003), Vol. 90.
[87] S. Lee, L. Jönsson, J. W. Wilkins, G. W. Bryant, and G. Klimeck, Phys. Rev. B **63**, 195318 (2001).
[88] S. Schulz, S. Schumacher, and G. Czycholl, Phys. Rev. B **73**, 245327 (2006).
[89] P. T. Różański and M. Zieliński, Phys. Rev. B **94**, 045440 (2016).
[90] M. Zieliński, Phys. Rev. B **88**, 115424 (2013).
[91] L. Jacak, P. Hawrylak, and A. Wojs, *Quantum Dots* (Springer, Berlin, 1998).
[92] Please note the reversed order of hole levels with respect to the electron.
[93] M. Świderski and M. Zieliński, Phys. Rev. B **95**, 125407 (2017).
[94] T. Smoleński, T. Kazimierczuk, M. Goryca, T. Jakubczyk, Ł. Kłopotowski, Ł. Cywński, P. Wojnar, A. Golnik, and P. Kossacki, Phys. Rev. B **86**, 241305(R) (2012).
[95] C. Tonin, R. Hostein, V. Voliotis, R. Grousson, A. Lemaitre, and A. Martinez, Phys. Rev. B **85**, 155303 (2012).
[96] E. Tsitsishvili, Physica E **87**, 161 (2017).
[97] Y. Léger, L. Besombes, L. Maingault, and H. Mariette, Phys. Rev. B **76**, 045331 (2007).
[98] M. Korkusinski and P. Hawrylak, Phys. Rev. B **87**, 115310 (2013).
[99] E. Poem, Y. Kodriano, C. Tradonsky, N. H. Lindner, B. D. Gerardot, P. M. Petroff, and D. Gershoni, Nat. Phys. **6**, 993 (2010).
[100] M. Gong, K. Duan, C.-F. Li, R. Magri, G. A. Narvaez, and L. He, Phys. Rev. B **77**, 045326 (2008).
[101] M. Zieliński, Nanoscale Res. Lett. **7**, 265 (2012).
[102] P. Klenovský, P. Steindl, J. Aberl, E. Zallo, R. Trotta, A. Rastelli, and T. Fromherz, Phys. Rev. B **97**, 245314 (2018).